Innovative Development of Next Generation and Energy Efficient Solid State Light Sources for General Illumination

Final Report
December 2006
Award Number: DE-FC26-03NT41954

Ian Ferguson
School of Electrical Engineering
Georgia Institute of Technology
Atlanta, Georgia 30332-250 U.S.A
Phone: 404-385-2885
Email: ianf@ece.gatech.edu

Abstract

A novel broadband spectrally dynamic solid state illumination source (BSDLED) has been developed that uses a dual wavelength light emitting diode (LED) and combinations of phosphors to create a broadband emission that is real-time controllable. Four major focuses of this work were as follows: (1) creation of a two terminal dual wavelength LED with control of the relative intensities of the two emission peaks; (2) bandgap modeling of the two terminal dual LED to explain operation based on the doping profile; (3) novel use of phosphor combinations with dual LEDs to create a broadband spectral power distribution that can be varied to mimic a blackbody radiator over a certain range; (4) investigation of novel doping schemes to create tunnel junctions or equivalent buried current spreading layers in the III-nitrides. Advances were achieved in each of these four areas which could lead to more efficient solid state light sources with greater functionality over existing devices.

Table of Contents

Table of Figures

Introduction

A novel solid state illumination source has been developed. A two terminal dual LED has been created with the ability to control the relative intensities of the two emission peaks by varying drive current. The development of a three terminal dual LED as a pump source was prohibited by the need for a III-nitride tunnel junction, that proved unattainable in the scope of this work. Doping profiles have been used to extend the dynamic range of the two terminal dual LED over other reported devices. Operation of the two terminal dual LEDs is explained as a function of drive current. In addition, novel use of phosphor mixtures allows the creation of a broadband spectral power distribution that can be varied using a dual LED as an excitation source. Combinations of phosphors that have varied excitation spectra provide the ability to selectively excite different phosphors with the different LED emission peaks. First and second generations of the two terminal dual LED and the phosphor combination are discussed. The final source has the ability to mimic the light of a blackbody radiator over a range of 3200 K - 5300 K.

Executive Summary

A functionally novel broadband white LED has been developed by using a dual wavelength emitter to preferentially pump phosphors in a mixture. The spectral power distribution (SPD) of the source can be dynamically tuned by varying the drive current of the device which can then be pulse width modulated to normalize the output intensity. A two terminal dual wavelength LED was used to pump a mixture of phosphors with varied excitation spectrum. One of the LED emission bands was used to preferentially excite part of the phosphor mixture while the second emission band was used to excite the remaining phosphors in the mixture. Varying the drive current of the LED allowed tuning of the relative intensity of the two LED emission bands. Careful selection of the phosphors and LED structure achieved a CCT range for the final device of 3200K – 5300K.

Several novel structures and materials were investigated and developed for use in the final device including: p-type doping schemes, transition metal doping of junctions, doping of quantum well barriers, phosphor combinations of varied excitation spectra. Two device designs were considered for the dual wavelength pump device. The first was a three terminal design incorporating a tunnel junction as a buried p-type contact. The extremely high p-type doping required for a suitable tunnel junction prohibited the use of the three terminal LED as a pump source. However, substantial work investigating novel p-type doping schemes was performed achieving hole concentrations above 1×10^{18} cm^{-3}. A novel hybrid doping scheme employed high and low temperature GaN:Mg layers to achieve high hole concentrations (~1×10^{18} cm^{-3}) while maintaining material quality (rms surface roughness < 10 Å). Tunnel junctions were achieved using hybrid p-type layer as the p++ layers; however, suitable performance (< 0.5 V @ 20 mA) for the tunnel junction reverse current was not achieved. Silicon and magnesium doped short period superlattice structures consisting of 5 Å periods of GaN/InGaN were also investigated as p++ layers. Hole concentrations ~ 3 x 1018 cm -3 were achieved; however, very little reverse current was observed when the SPS layers were incorporated into a tunnel junction structure.

The final dual wavelength LED employed was a two terminal LED consisting of 3 quantum wells (QW) designed to emit at ~460 nm followed 3 QWs designed to emit at 400 nm. The barrier between the third and fourth QWs was doped with silicon to limit hole injection across the barrier and enable control of the carrier recombination in each QW region. Controlling the carrier recombination allowed for control of the SPD of the LED. The variation range for the LED was less than that that could be achieved with a three terminal device, but was suitable for pumping the phosphors chosen.

The final phosphor combination incorporated 5 phosphors including a UV-to-white, green, YAG, orange and red. The final phosphor combination was developed to work with the two terminal dual wavelength LED and achieved a CCT range of 3200K-5300K.

Efficiency in these devices is not expected to be drastically different from other high brightness LEDs because the fundamental processes are not drastically changed. On the other hand some gain in efficiency could be seen by properly choosing phosphors and pump wavelengths to minimize stokes shift losses seen in other phosphor converted LEDs. Further optimization of the two terminal dual wavelength LED will achieve the most efficient operating point and minimize the amount of drive current variation needed

to tune the SPD. Finally, optimization of these devices can enhance solid state light sources and potentially increase the efficiency of phosphor converted LEDs.

Experiments + Theory

The development of the broadband spectrally dynamic required a number of other developments including a phosphor combination, dual wavelength LED and a tunnel junction. Several experiments for each of these structure are described. Novel p-type doping schemes were a major part of the work.

High hole concentrations in GaN are difficult to achieve due to the high thermal ionization energy (~180 meV) of Magnesium (Mg) in GaN. At room temperature less than 1% of Mg acceptors are typically electronically active. Therefore, in order to achieve acceptable hole concentrations, high Mg incorporation far above normal doping densities is required. This high doping concentration, however, decreases the crystalline quality of the film, which consequently increases its resistivity and makes it difficult to obtain good electrical contacts to the material. Resistive films cause current crowding in LEDs. A semitransparent contact is deposited onto the entire surface of the p-type region to compensate for current crowding; this is followed by a smaller but thicker bonding pad. The cost of using this semitransparent current spreading layer is a reduction in light extraction from the device by not entirely transmitting the incident light. Post-growth treatment of GaN:Mg is another important issue. Typically, material is annealed in a non-H_2 environment to break the compensating Mg-H bond that occurs in metal organic chemical vapor deposition grown GaN:Mg. Reports show that optimization of the annealing process can lead to more effective activation of Mg acceptors. Some reports suggest that annealing in air (containing O_2) can further increase Mg activation in GaN[1].

Current crowding poses a problem for buried p-type contacts in an LED. It is not possible to deposit a metal current spreading layer similar to a top p-type contact and a simple bonding pad will not provide enough current spreading for an efficient device. Hence, a tunnel junction is one solution to contacting buried p-layers. In this work, p+ GaN layers have been developed for use in a tunnel junction that may be used in two and three terminal devices for solid state lighting applications.

Tunnel Junction Theory

Electron tunneling results from a quantum mechanical phenomenon from the wave nature of electrons [2]. When an electron wave is incident with energy less than the energy barrier height, there is a probability that this electron can penetrate this energy barrier, and the penetration depth depends on the barrier height. Figure 1 shows a rectangular barrier with potential height of V, and thickness of d.

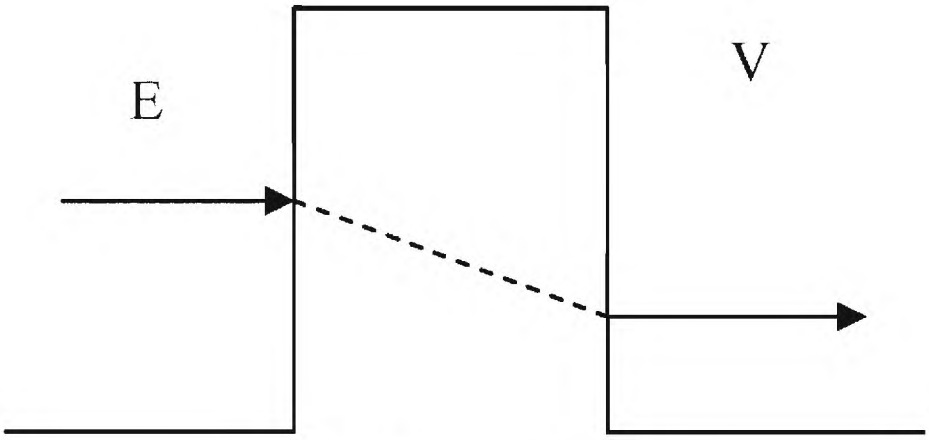

Figure 1. Potential barrier seen by an electron.

For an electron wave with energy E_v, the tunneling probability is given by Equation 1:

$$T(E_v)=\left[1+\frac{V^2 sinh^2(kd)}{4E_v(V-E_v)}\right]^{-1}, k=\sqrt{\frac{2m(V-E_v)}{\eta^2}} \quad (1)$$

where m is the effective mass of an electron, ħ is the plank constant. The tunnel probability is high for very thin barriers. For arbitrary shape of potential barriers, a numerical solution can be obtained by approximating the potential barrier with multiple sub-potential layers, each sub-potential layer can be treated as a constant potential layer. Equation 1 is used to calculate the tunneling probability for each of these constant potential barriers.

In semiconductor materials, carriers can be generated by band to band tunneling when a strong electric field presents, for example, the electric field greater than 10 mV/cm. For a reversed biased, heavily doped, thin pn junction, if the electron penetration depth is larger than the depletion width of this pn junction electrons at valence bands at p side can penetrate into conduction bands at n side to become free carriers. This is the so called tunneling junction. The uses of a tunnel junction (TJ) in III-Nitride LEDs have been demonstrated recently [3]. The reverse biased TJ is to improve the lateral current spreading. With a TJ, n-GaN can be used to replace p-GaN as a top cap layer. Commonly, a so called semi-transparent p-Pad is usually applied on the top of p-GaN to overcome the low conductivity of p-GaN In conventional LEDs. The n-GaN has much higher conductivity, about 100 times, compared to p-GaN , and the reverse biased TJ supplies holes to p-GaN adjacent to the active region through lateral current. As a result, the application of n-GaN top contact layer can improve the current spreading of the LED, and increase light extraction by avoiding using semitransparent contact. Another benefit of using a TJ is the simplification of the LED fabrication process because n-GaN can be used as to implement both the top p-contact and lower n-contact as shown in Figure 2.

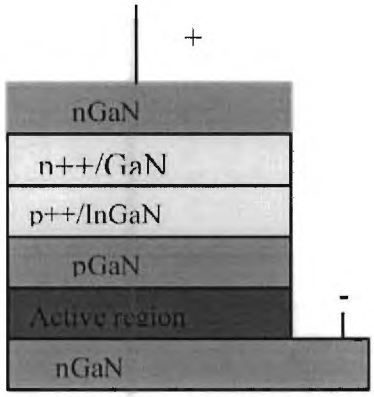

Figure 2. Structure of a tunnel junction

The TJ usually is fabricated using heavily doped p++/n++ either InGan/GaN or GaN/GaN bi-layer. One example use an InGan/GaN bi-layer with layer thicknesses of 15 nm/30nm [4]. The p-type doping Mg level is about 10^{20} cm^{-3}, and n-type doping Si level is about $6x10^{19}$ cm^{-3} for this tunneling junction. This TJ is incorporated into a resonant cavity LED with violet light emission. The resonant cavity of this LED uses two pairs of DBRs: the top one is a SiO_2/HfO_2 above the TJ, and the bottom one is an AlGaN/GaN DBR grown on a GaN buffer layer. A TJ in the second example is fabricated using a GaN/GaN layer with layer thicknesses of 10nm/10 nm. The p+ GaN layer is doped with $3x10^{19}$ cm^{-3} of Mg; the averaged Si doping level in the n+ GaN layer is about $10^{20}cm^{-3}$. A n-GaN is grown on the top of this TJ to replace the conventional p-GaN as a top contact layer. One disadvantage of the TJ is its large forward voltage, about 1 volt higher than that of a conventional LED because the TJ add a series resistance to the LED. However, the overall optical power of a LED is claimed to double compared to the conventional LED with a top semitransparent p-Pad[3]. A necessary characteristic to tunneling is the negative differential resistance (NDR) region in the forward bias operation of a tunnel diode, because it shows the existence of band-to-band tunneling (Figure 3)[5].

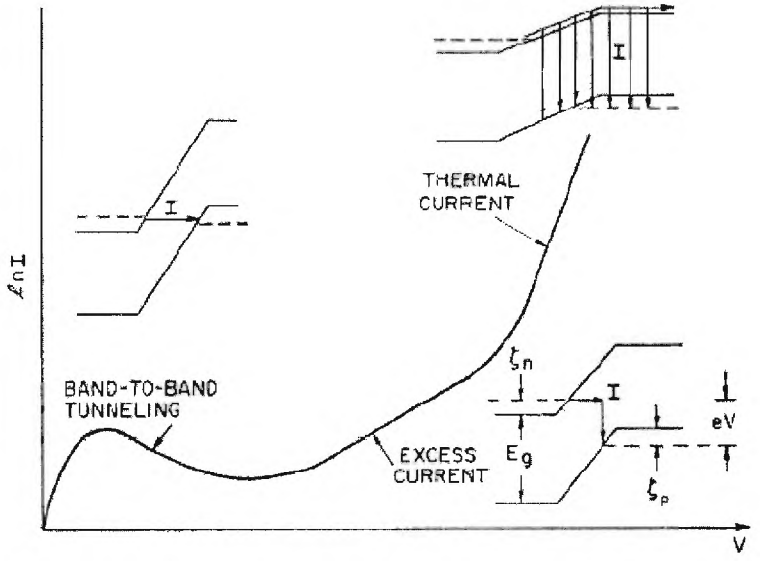

Figure 3. Current-voltage characteristic of a degenerate p-n junction

In the NDR region a decrease in the density of states leads to a decrease in tunneling probability and a subsequent decrease in current density [6]. Kane derived an equation for the current density of a tunnel diode as shown in Equation (2) [6].

$$j_t = \frac{em^*}{18\eta^3} e^{\frac{-\pi\sqrt{m^*}E_G^{\frac{3}{2}}}{2\sqrt{2}\eta F}} \left(\frac{\overline{E}_\perp}{2}\right) \times \int [f_1(E_1) - f_2(E_2)] \left[1 - e^{\frac{-2E_s}{\overline{E}_\perp}}\right] dE \qquad (2)$$

where E_s is the smaller of E_1, E_2. Kane's work will be used as a basis for understanding and quantifying the observed tunneling mechanisms in the GaN device. Full analysis of the current-voltage characteristics will lead to a better understanding of the device, although tunnel junctions for this work will be operated in the reverse bias region. A better understanding of GaN based tunnel junctions will help to optimize them for incorporation as more efficient contacting layers in LEDs. Currently, the presence of a tunnel junction increases the series resistance of the device by 33% [7] over a typical LED with semitransparent current spreading layer. A goal of this research will be to reduce the series resistance of GaN tunnel junctions.

Hybrid p-type Doping

Hybrid doping was the first doping scheme employed in the tunnel junction development. Three sets of runs were performed to optimize hole concentration and material quality. The first set of growths was at high temperature (~1030°C) in which the molar flow ratio of Cp_2Mg/TMGa was changed from 0.00556 to 0.0667 in order to incorporate more Mg into the films and maintain a high quality epitaxial layer. The second set of runs repeated the change in molar flow ratio of Cp_2Mg/TMGa from the high temperature runs, but with a lower deposition temperature (~980°C). The third set of growths, hybrid p-type doping, consisted of alternating layers of high and low temperature p-type GaN repeated 10 times. The high temperature layers were doped with a molar flow ratio of 0.0334 Cp_2Mg/TMGa, while the low temperature layers were highly doped with a molar flow ratio of 0.0459 Cp_2Mg/TMGa. It is important to note that in the first and second set of growths the molar flow ratio was set by changing the Cp_2Mg flow and maintaining a consistent TMGa flow. However, in hybrid p-type doping, the molar flow ratio was set by changing either the TMGa flow or the Cp_2Mg flow. It is believed that decreasing the amount of available gallium allows for higher rates of Mg incorporation. For all growths, NH_3 flow was held constant.

Several tunnel junctions were grown where the p++ layer was varied according to the three sets of growth runs described in this work (a general schematic of the devices is shown in Figure 4).

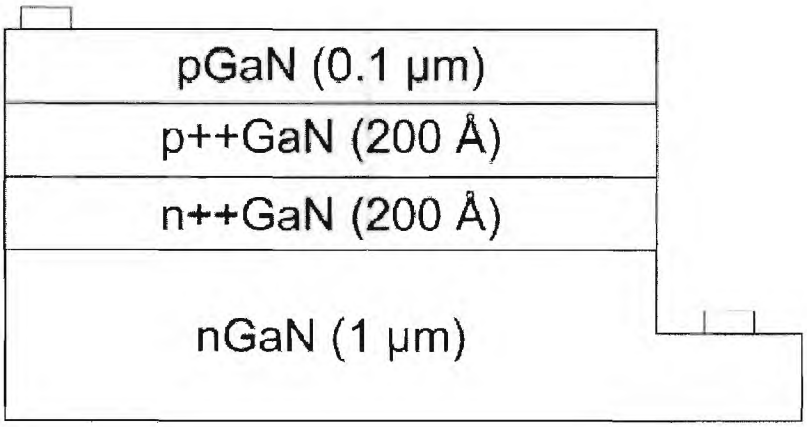

Figure 4. Schematic of the layer structure used in tunnel junction growths

A GaN buffer layer was grown on top of a bare sapphire substrate at low temperature (500°C to 600°C) followed by high temperature (~1050°C) undoped GaN and then an n-type GaN with SiH_4as an n-type dopant at a molar flow ratio of 3.51 to TMGa. The TMGa was switched with TEGa for the n+ layer (highly doped n-type GaN), which was grown at low temperature (~980°C), and SiH_4 was used as an n-type dopant at molar flow ratio of 48.3 to TEGa. To ensure a better interface between the n+ and p+ layers a thin layer of undoped GaN was introduced as a barrier to magnesium diffusion. The device was capped with high quality p-type GaN.

The activation process was also changed, in addition to varying the temperatures and molar flow ratios of Cp_2Mg/TMGa. A standard rapid thermal annealing (RTA) process was used at 800°C with N_2 ambient. Also, lower temperature (500°C) atmospheric anneals were performed after some reports indicated that oxygen could enhance the activation process [1]. The atmosphere anneals were done at times ranging from 5 minutes to 3 hours.

Secondary Ion Mass Spectroscopy (SIMS) was used to measure Mg incorporation in the layers. Hall measurements were used to determine hole concentration and atomic force microscopy was used to measure surface quality. Scratch diodes and lithographically fabricated diodes were used to test for tunneling in the tunnel junction devices.

III-Nitride Tunnel Junctions with Hybrid Doping

III-nitride tunnel junctions were grown by MOCVD. Various novel doping schemes to create highly doped p-type GaN were employed with Mg as the acceptor ion. Highly doped p-type material (p++) is necessary for creating efficient tunnel junctions that act as buried current spreading layers and provide high quality contacts to p-type GaN. Molar flow ratios and growth temperature were varied to achieve maximum doping concentration. SIMS and Hall Effect were used to measure Mg incorporation and carrier concentration, respectively. The maximum carrier concentration achieved employed a

hybrid growth scheme that achieved high carrier concentration and high quality material by alternating layers of high and low growth temperature material. The hybrid growth scheme developed here is a novel growth process that enhances p-type GaN. Successful GaN tunnel junctions were grown using the hybrid p-type doping scheme developed in this work. I-V measurements were taken on these devices to evaluate the effectiveness of the devices.

Short Period Superlattice Doping

GaN/InGaN short period superlattice (SPS) structures doped with Si or Mg were investigated as possible doping schemes for a III-nitride tunnel junction. SPS structures have been suggested as and reported to have the potential for achieving higher carrier concentrations than bulk layers. The superlattices in this work had periods of 5 Å GaN and 5 Å InGaN. The test structures were each comprised of 20 periods. Hall and PL spectroscopy measurements were performed on the SPS test structures to evaluate their quality. Junctions were then grown using the Mg doped SPS and Si SPS structures and evaluated as tunnel junction devices

SPS test structures were grown with varying levels of silicon and magnesium doping. The test structure consisted of 20 periods of alternating Si/Mg:InGaN and GaN layers of 5 Å thickness grown on top of 1.5 μm of undoped GaN on a sapphire substrate. Both the InGaN and GaN layers were grown at ~800°C, which is the normal growth temperature for InGaN. However, high quality GaN is normally grown at ~1000°C. In this structure the quality of the material is preserved as characterized by AFM, XRD, and PL.

Mn Doping

Mn doping was introduced into a tunnel junction structure similar to the one mentioned previously that used the hybrid p-type doping scheme to assess its effect on tunneling behavior. Mn dopants tend to have energy levels in the middle of the bandgap for GaN, which may lead to defect enhanced tunneling. Normally, as the tunnel junction is driven in to reverse bias, tunneling may occur when the valence band of the p-side is at higher potential than the conduction band of the n-side. The tunneling probability is a function of the width of the tunnel barrier, however, if a state exists in that barrier it may act as a transition point for carriers, and improve the tunneling probability as shown in Figure 5.

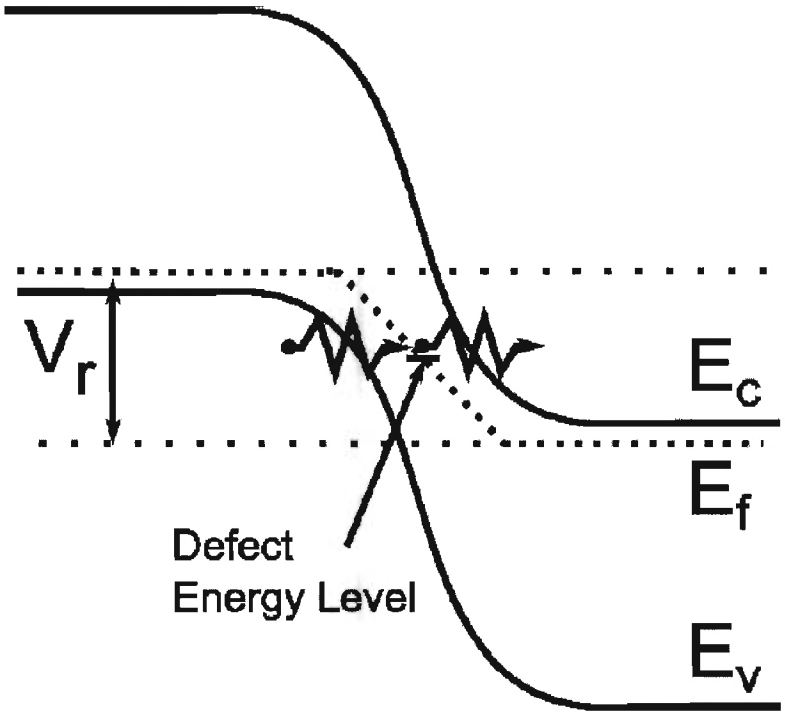

Figure 5. Tunnel junction in reverse bias illustrating defect assisted tunneling

Several devices were grown and fabricated. The layer structures shown in Figure 6 are modified from the tunnel junctions employing the hybrid doping scheme mentioned before.

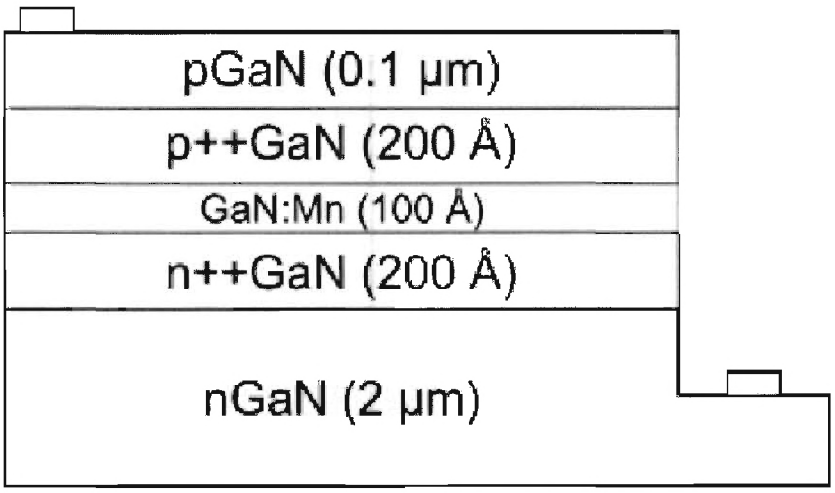

Figure 6. Tunnel junction structure schematic showing GaN:Mn placement

Phosphor Test Bed

First Generation Phosphor Test Bed

The basis for a BSDLED was demonstrated by pumping a combination of phosphors with multiple wavelengths of excitation, and then varying the relative intensities of those pumps. Such a device is a novel concept and will play an innovative role in solid state general illumination.

A wide variety of phosphors that are excited by a range of pump wavelengths exists. In fact, a single phosphor may respond differently to different pump wavelengths. Thus, a combination of multiple phosphors with differing and exclusive excitation spectra can be simultaneously pumped by multiple wavelengths to produce white light. The relative intensities of the pump peaks can then be varied to change the output of the total device and therefore allow dynamic tuning of the correlated color temperature (CCT). Such a device combines the controllability seen in RGB-LEDs and the broadband characteristics of PC-LEDs. It is believed that such innovations will prove instrumental in the success of solid state general illumination sources that require high quality dynamic white light.

Second Generation Phosphor Test Bed

A wider range of phosphors were combined to create a mixture that would have CIE coordinates closer to the Planckian Locus. In addition to the phosphors used in the first generation test bed, YAG:Ce and an orange emitting phosphor were used to enhance the spectral power distribution of the source. Another stipulation to the second generation phosphor test bed was that it work with the second generation dual LEDs described below. These devices do not have the dynamic range that is achievable with two discrete devices, which can have β ranging from 0 to ∞.

Dual LEDs

First Generation Two Terminal LED Structures

LED structures with multiple quantum well regions designed to emit at different wavelengths have been grown. It has been observed that the emission mechanism for each of these MQW regions is the same as that seen in a single MQW region LED. Dual MQW region LEDs, Figure 7, for efficient pumping of multiple phosphors have been grown by MOCVD for use in broadband, white solid state light sources.

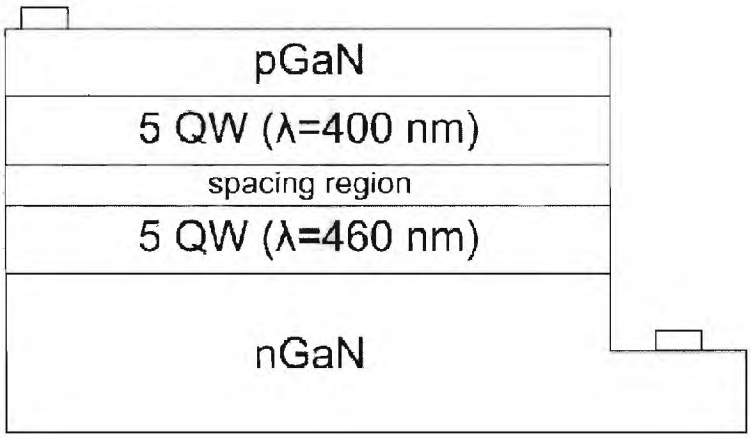

Figure 7. Layer schematic of 1st generation Dual LED

Blue (460 nm) and Violet/UV (~400-420 nm) emitting MQW regions were incorporated into a single device and show recombination mechanisms similar to single MQW region devices. The introduction of a spacing region successfully separated the electroluminescent emissions, and two distinct emission peaks were observed. A large factor in the efficient radiative recombination in these devices is the localization of carriers by indium compositional fluctuations in the InGaN quantum wells. Photoluminescence measurements were carried out to determine the physical mechanism behind light emission in these devices. Optical recombination in low-dimensional InGaN quantum structures strongly depends on the localization of carriers in quantum dot-like structures[8,9,10,11]. Inhomogeneities in the indium concentration on the nm-scale provide potential fluctuations in the band gap, and the carriers are trapped in islands that may provide 3D-quantisation up to elevated temperatures [10]. An increased overlap of hole and electron wave functions is induced by the localization of carriers in the nanoscale islands. The average localization energies were determined by an Arrhenius plot of the luminescence intensity following the approach suggested by Adelmann et al [12]. The two activation processes are necessary to describe the data in both low and high temperature regimes.

All the LEDs in this work consisted of InGaN/GaN quantum wells in the active region. The emission wavelength was controlled by changing the growth temperature of the wells, which affected the growth rate and the indium incorporation. The barrier was grown in two stages; the first stage was grown without hydrogen and the second stage was grown with hydrogen and at a higher temperature and rate than the first stage. Multiple growths were completed to optimize the growth rate of the well and the two stage barrier.

A series of systematic growth runs were completed at various temperatures to better understand the effects of temperature on the indium incorporation in the quantum wells. Active regions were developed specifically for 460 and 400-420 nm emission. X-ray diffraction and structure simulation were used to study changes in the indium concentration with respect to the growth temperature and the thickness of the wells against the emitted and PL wavelength.

Next, a series of devices containing a 460 and a 400-420 nm set of multi-quantum well regions, a dual MQW region structure, separated by an undoped spacing region was grown as shown schematically in Figure 7. The dual MQW region emitter incorporated the optimized MQW growth conditions for the respective emission wavelengths. The device structure development focused on the 3 layers shown below:

- First set of MQW (460 nm)
- Spacing layer between the two MQWs
- Second set of MQW (400-420 nm)

The 460 nm MQW was placed at the bottom so that it does not reabsorb the emission from the 400-420 nm MQW. A spacing layer was introduced between the two MQWs to mitigate interaction. The two respective MQWs were split into three growth stages: the quantum well and a two stage barrier. As discussed above, temperature was used to vary the indium incorporation into the well to control the desired emission wavelengths. During device optimization it was determined that varying well and barrier thickness and different growth temperatures were the best approach for the two sets of MQWs.

Thin and thick undoped GaN, n-type GaN and low aluminum concentration GaN layers were studied for the spacing layer at both low (below 800°C) and high (above 900°C) temperature growths. In addition, different precursors for gallium (TMGa and TEGa) were evaluated to optimize the interface layer.

Second Generation Two Terminal Dual Wavelength LEDs

The first generation of two terminal dual wavelength had an emission spectrum with two distinct peaks which could be used to efficiently couple into multiple phosphors of different excitation spectra. However, dynamic control of the relative intensities of the two peaks was limited in these devices. A second generation of devices were designed to increase the ability to control the relative intensity of the two peaks and simplify the structure. A series of experiments were performed to determine the behavior of these devices. A basic schematic of the device layer structure is shown in Figure 8.

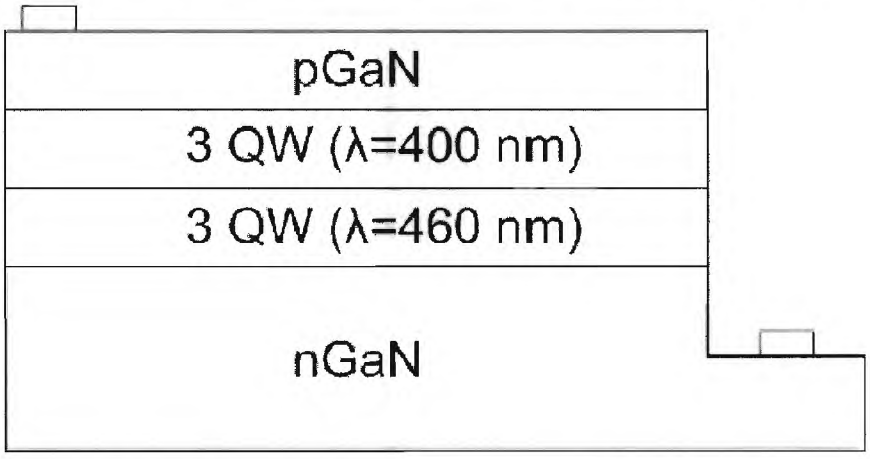

Figure 8. Layer schematic for 2nd generation Dual LEDs

The samples were grown in the highly modified commercial MOCVD reactor used for the rest of the work. The active region consisted of six quantum wells with three designed to emit at 400 nm and three designed to emit at 460 nm. The first three grown were designed to emit at 400 nm and will be referred to as QWs 1-3, while the last three grown were designed to emit at 460 nm and are referred to as QWs 4-6. Below the active region is an n-type GaN region with carrier concentration of $10^{18}cm^{-3}$ electrons. Above the active region a p-type GaN region with hole concentration $10^{17}cm^{-3}$. The n and p-type regions used in these device are typical of common LED structures. In this study the most important metric was the relative intensity of the two emission peaks. β is defined as the ratio of the long wavelength intensity to the short wavelength intensity. In the case of these samples the long wavelength quantum wells are positioned nearer the n-type GaN layer and the short wavelength quantum wells are positioned near the p-type gallium nitride. In effect, β is a measure of the amount of electron hole pairs recombining in the long wavelength quantum wells as compared to the short wavelength quantum wells, which is dependent on the current injection into both of those regions. β will be used throughout this section to denote this ratio in the text and figures.

Results and Discussion

Hybrid p-type Doping

The variation of Cp_2Mg/TMGa ratio at high temperatures had little effect on hole concentration as measured by Hall effect or Mg incorporation as measured by SIMS. At higher deposition temperatures with Mg incorporation of $5x10^{19}cm^{-3}$, hole concentrations of $1x10^{17}cm^{-3}$ were achieved for RTA and atmospheric annealed samples, and surface morphologies remained good, up to a Cp_2Mg/TMGa ratio of 0.0459 as shown in

Table 1.

Table 1. Summary of p-GaN doping data

Mg/Ga Precursor Flow Ratio	0.014	0.050	0.100	0.025 (HT)/ 0.045(LT)
RMS Roughness (Å)	3.3	9.7	25.5	7.2
Hall Effect (cm^{-3})	$1x10^{17}$	$3x10^{17}$	$2x10^{18}$	$2x10^{18}$
AFM Scan (4μm x 4μm)	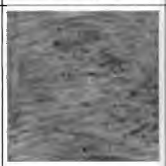		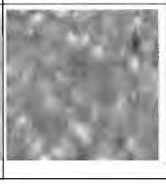	

However, at lower deposition temperatures with Mg incorporation of $1x10^{20}cm^{-3}$, hole concentrations $>1x10^{18}cm^{-3}$ were achieved with atmosphere annealing and increased Cp_2Mg/TMGa flow ratio, but these samples exhibited poor surface morphology. Finally, the hybrid p-type doping, described above, achieved good surface morphology and hole

concentrations $>10^{18}cm^{-3}$ using the standard RTA activation process, while no atmospheric annealing was performed on these samples as mentioned in the preceding section. In the hybrid doping, the balance between the Mg incorporation and the surface quality depended on the TMGa molar flow and the layer thickness of the respective temperature growths. Different Cp_2Mg molar flows were evaluated for the high and low temperature growth layers while keeping the TMGa molar concentration constant, but regardless of temperature they lead to poor surface quality and thus poor contacts. Lowering the Cp_2Mg molar flow greatly improved the surface quality, but it also reduced the carrier concentration and a working tunnel junction could not be achieved. A substantial improvement in the carrier concentration, from $1x10^{17}cm^{-3}$ to $1x10^{18}cm^{-3}$, without diminishing surface quality was seen when the Cp_2Mg molar concentration was kept constant for both the low temperature and high temperature layers, while the TMGa molar concentration was reduced for the low temperature layers.

Tunnel junctions employing p+ layers from each of the three growth runs exhibited different properties. Junctions with a high temperature p+ layer exhibited no tunneling, only typical diode behavior; this was true for both annealing processes. On the other hand, low temperature p+ layers showed tunneling when the sample was atmosphere annealed, but not after the standard RTA, Figure 9.

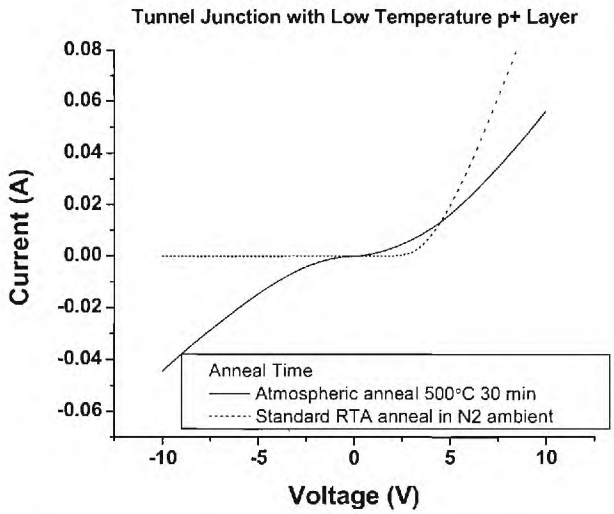

Figure 9. Comparison of an atmosphere anneal to standard RTA, and its affect on p+ layer, and tunneling

RTA under a N_2 ambient showed no effect on surface morphology as viewed under an optical microscope. Conversely, the atmosphere annealing caused a deterioration of the surface and was not used with the hybrid doped devices. Diodes (tunneling and normal) processed with the atmosphere anneal showed higher resistance.

Discussion of Hybrid Doping

The first method for p+ doping did not allow for enough Mg incorporation into the GaN. Ga incorporation is more efficient at higher temperatures, blocking the incorporation of Mg. However, the quality of GaN is preserved, as observed by surface

inspection. At lower growth temperatures it is possible to incorporate more Mg and activate more acceptors, but the quality of the crystal surface tends to deteriorate. If the lower temperature p+ layers are used as a buried contact, the overgrown layers suffer from poor crystallinity, and a complex device becomes impossible.

Hybrid doping of the p+ region combines the good crystallinity of higher temperature GaN:Mg with the higher doping potential of low temperature materials. Higher Mg incorporation rates are achievable, by decreasing the TMGa flow relative to the Cp_2Mg flow, due to the lack of available Ga that would normally prevent Mg incorporation. In addition layers with high Cp_2Mg/TMGa molar ratios were kept thin to minimize disturbance to the crystal. Tunneling was achieved as shown by the I-V curves and the N-type negative resistance exhibited in Figure 10.

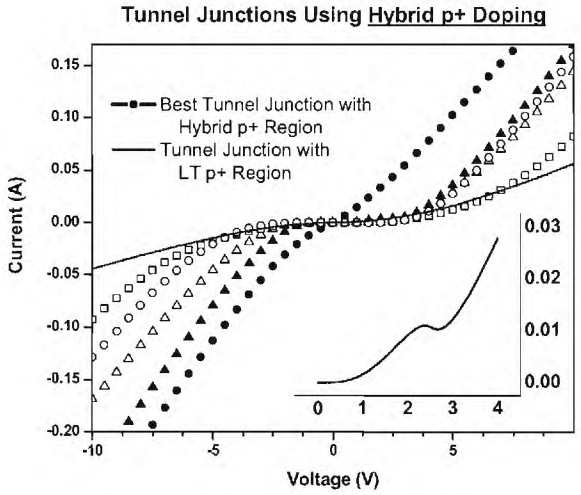

Figure 10. Current-Voltage data for several Tunnel junctions using the hybrid growth scheme

Such a device is a good candidate for a buried contacting and current spreading layer in other devices, eliminating the need for the p-type material to be the top layer. Tunnel junctions have also been demonstrated as fully transparent current spreading layers on the top of devices [3].

Atmospheric annealing in normal atmospheric conditions was also evaluated as a way of increasing the activation of Mg in GaN. While some improved carrier concentrations were observed with Hall measurements, a tradeoff came in material quality deterioration. Although there may be some optimal condition for activation without unacceptable material degradation, such a method is unsuitable for a buried p+ layer, because it is essentially capped from the oxygen that is believed to cause higher activation efficacy.

Short Period Superlattice Doping

Si Doped SPS Structures

AFM measurements provide a RMS surface roughness of 10 Å, while Figure 11 is PL data for the SPS structure showing a GaN peak at 3.4 eV. Hall effect measurements showed electron carrier concentrations in excess of $1x10^{20}cm^{-3}$.

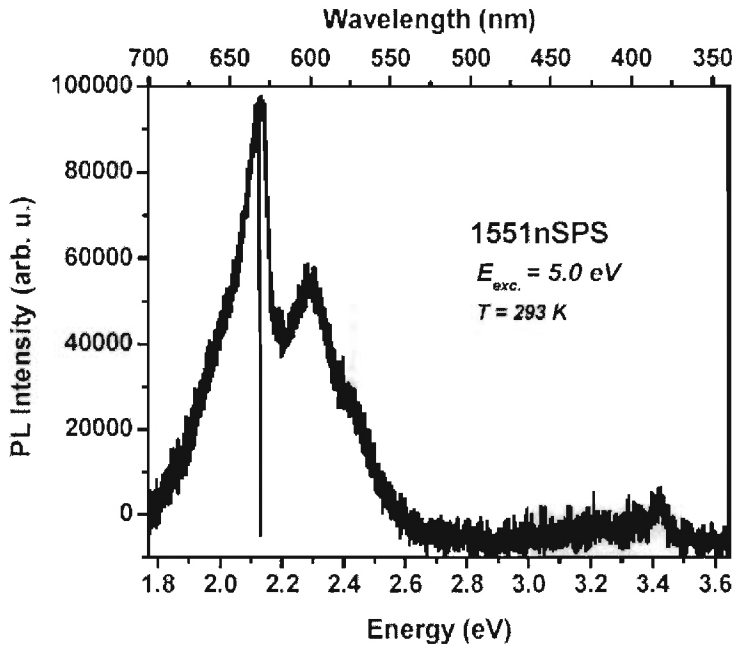

Figure 11. PL Spectrum for nSPS test structure

Mg Doped SPS Structures

Magnesium doping was introduced instead of silicon to investigate the properties of a pSPS structure. The growth was performed at 800°C for both the GaN and InGaN. The doping concentration was maximized using feedback from PL spectroscopy and Hall effect measurements. PL spectra of three samples are shown in Figure 12, Figure 13 and Figure 14.

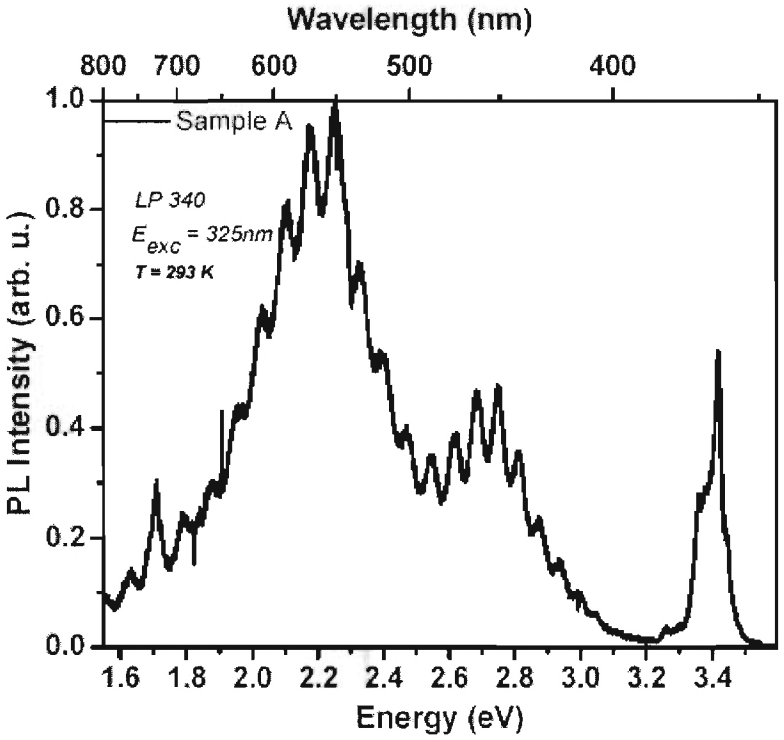

Figure 12. PL spectra of baseline pSPS doping

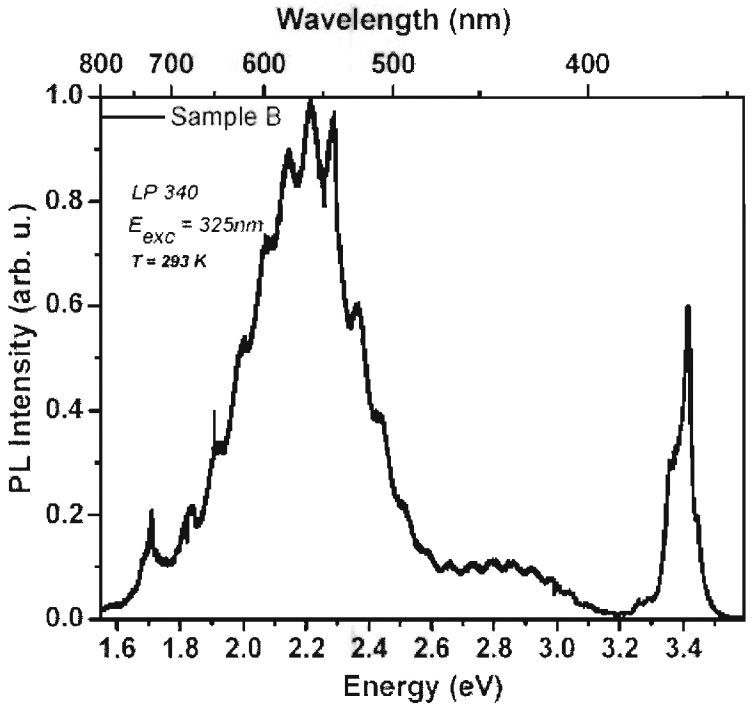

Figure 13. PL spectra of twice baseline pSPS doping

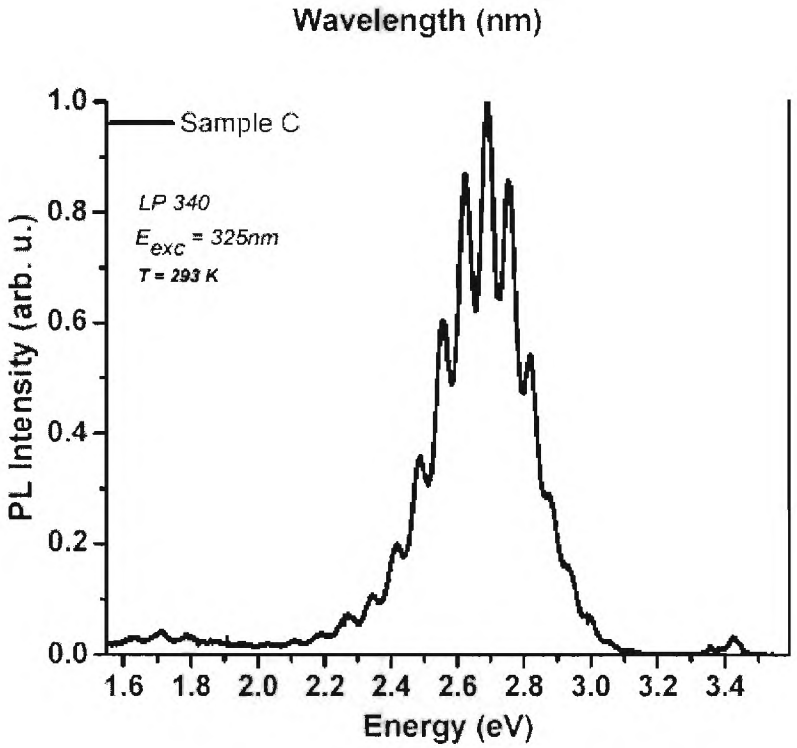

Figure 14. PL spectra of half baseline pSPS doping

The flow of Mg into the chamber during growth is the only difference in these structures. The growth was performed at 800°C for both the GaN and InGaN. Sample A is shown as a baseline doping concentration. Sample B has twice the Mg flow and Sample C has half the Mg flow. Each of the PL spectra shows strong Fabry-Perot oscillations indicating high quality interfaces in the superlattice. Each spectra also shows a peak near 2.8 eV arising from the superlattice InGaN composition. Samples A and B have another peak in their spectra that is due to defects in the material from over doping of Mg. The relative intensity of the defect band to the SPS peak indicates the level of defects in the material. For instance, in sample B which has twice as much Mg flow as sample A, the defect band nearly washes out the SPS peak. However, in sample C there is no defect band, indicating that there is no overdoping from Mg. This explanation is corroborated by the results of Hall measurements shown in Table 2.

Table 2. Hall measurements for p-GaN samples

	Sample A	Sample B	Sample C
Hole Concentration	1.99×10^{18}	8.86×10^{17}	3.65×10^{18}
Mg Flow	Baseline	Twice	Half

Carrier concentrations for pSPS samples The hole concentration for sample C is higher than that of samples A and B which indicates that the samples are suffering from compensation effects from over doping of Mg.

SPS junctions

The SPS test structure described in the previous sections were then used to form a pn junction. Two variations of the structure are shown in Figure 15.

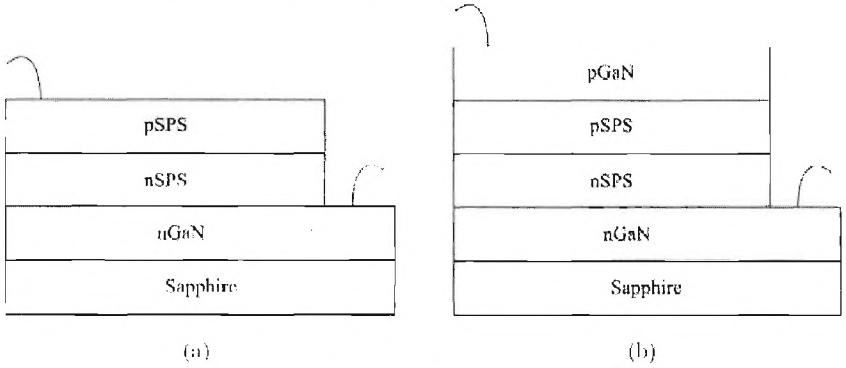

Figure 15. Schematics of two variations of SPS junctions

The n SPS layer was the same as above and the pSPS layer was the same Sample C. Current voltage measurements were performed on the devices to assess them as tunnel junctions, however, very little reverse current could be achieved. It is unclear whether further optimization of these structures would lead to a tunnel junction.

Mn Doped Junction

Mn has been introduced into the intrinsic region at the junction between the n++ layer and p++ layer. Table 3 shows the expected Mn concentrations in each of the samples. All other paramters were held constant except the flow of Mn entering the reactor.

Table 3. Summary of Mn-GaN doping parameters

Sample	Mn Concentration
Low Mn Doping	.5%
Medium Mn Doping	1%
High Mn Doping	2%

Mn doping for tunnel junctions The current voltage results are shown below in Figure 16.

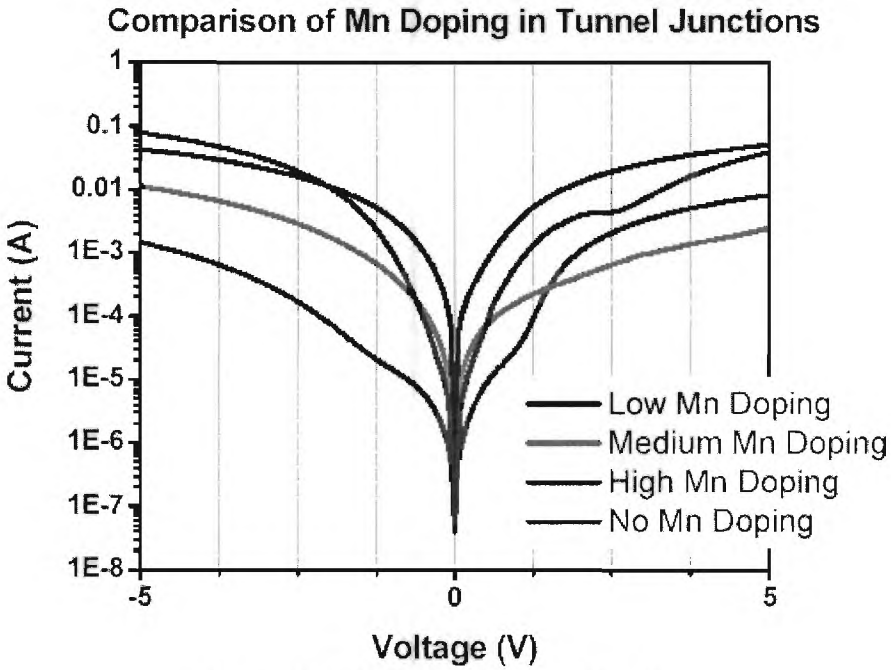

Figure 16. I-V plots of Mn Tunnel junctions

It can be seen that each of the samples containing Mn in the junction has reduced reverse current as compared to the junction without Mn. One explanation for this is that the presence of Mn impurities in the junction increases carrier scattering causing more carriers to give off their energy in the form of photons. A more plausible explanation maybe that the Mn impurities diffused into the p++ layer partially compensating the hole concentration resulting in a fermi level further away from the valence band. A decrease in the p-type doping would increase the tunneling barrier seen by carriers as and decrease the amount of tunneling current.

Phosphor Test Bed

First Generation Phosphor Test Bed

The analyses of several phosphors for use in a dynamic phosphor converted illumination source are reported here. Such a device can be constructed using readily available phosphors and pumped with standard GaN LED emission wavelengths. Pump wavelengths of 400 nm and 460 nm were chosen based on a number of criteria including availability of phosphors and desired output spectrum. The phosphors analyzed here include: UV to white (A), $SrGa_2S_4$ (B), SrCa:Eu (C). Each phosphor was excited by the 400 nm and 460 nm light independently and simultaneously and the output power spectra observed. Phosphor A was strongly excited by 400 and not 460, while the converse was true for Phosphor C as shown in Table 4.

Table 4. Summary of phosphor excitation data

Excitation	Phosphors		
	$SrGa_2S_4$ (Green)	SrCa:Eu (Red)	UV to White
460 nm	Strong	Strong	Weak
400 nm	Strong	Weak	Strong

Phosphors A, B and C were then combined based on the results in Table 4 to achieve a source with CCT similar to an incandescent bulb. Next, the dual wavelength source was used to excite the phosphors as the relative intensities of the two wavelengths were varied from singular 460 nm or 400 nm pumping to equal pumping from both wavelengths. Figure 17 a and b shows the change in phosphorescence as the intensity of one wavelength is held constant and the other varied for both cases.

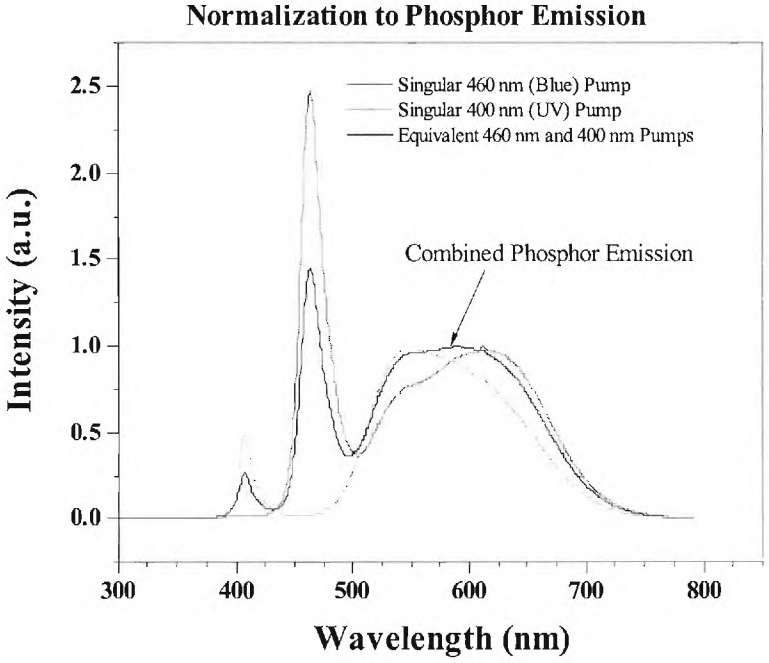

Figure 17. Phosphorescence for changing 460 nm and 400 nm pump

The shape of the emission curve is shown to change by varying the relative intensity of the two pump wavelengths. Figure 17 shows an increase in the red phosphorescence (~655 nm peak) as the 460 nm pump relative intensity is increased (red curve). In addition, Figure 17 shows that an increase in 400 nm relative intensity is accompanied by an increase in the yellow/green (~560 nm peak) phosphorescence (green curve). Finally, the black curve represents equal pumping intensity by both pumps.

Figure 18 shows the varied spectra plotted on a 1931 Commission Internationale De L'eclairage (CIE) diagram showing the variation of chromaticity achievable with this combination of phosphors.

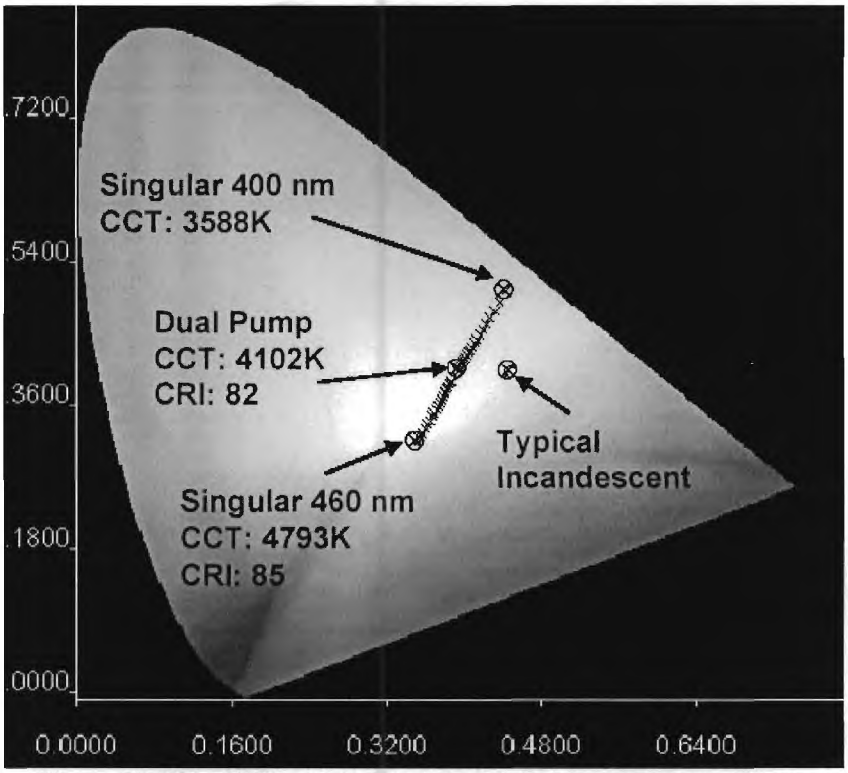

Figure 18. Plot of CIE coordinates for varied phosphorescence spectra

Pumping relatively harder with the 400 nm light excites more of the yellow/green phosphor emission moving the chromaticity coordinates closer to the yellow edge of the spectrum. Increasing the relative intensity of the 460 nm pump excites more of the red phosphorescence as well as adding blue light from the pump to the spectrum, thus, shifting the chromaticity coordinates toward the violet edge (bottom left) of the CIE diagram. A large range of points can be accessed with this combination of phosphors and pump choices. In addition, correlated color temperatures (CCT) ranging from 3588 K to 4793 K are achievable. Another important note is the high color rendering index (CRI) of 85 and 82 as listed in Figure 18. These CRIs rival many fluorescent lamps and are attributed to the broad emission from the combined phosphor emission.

These results show great potential for BSDLEDs. Such a source is possible by using a three terminal device as described previously and phosphor combinations similar to those analyzed here. Innovations such as this will help solid state illumination sources gain a competitive advantage over conventional illumination sources. This will be necessary for solid state lighting to realize success in the general illumination market.

Second Generation Phosphor Test Bed

YAG responds very well to pumping with 460-470 nm light, but not to ~400 nm light. On the other hand, the orange phosphor used responded equally well to pumping from 400-480 nm light. The range of chromaticity achievable with the second generation phosphor combination is shown in Figure 19.

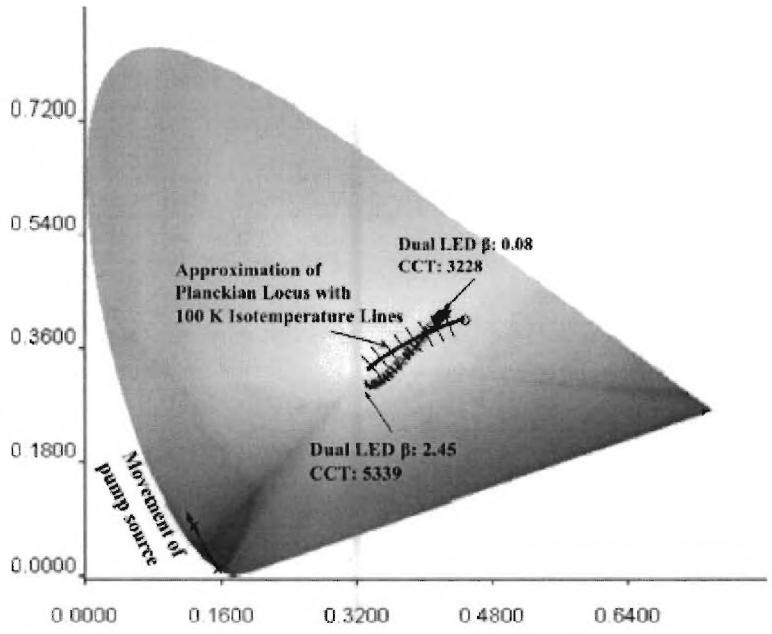

Figure 19. CIE daigram with range of second generation phosphor mix

This was achieved using the two terminal dual LED described later. When β of the source is 0.08, the spectrum has a CCT of 3228K, and is very similar to an incandescent light bulb. As β is increased by increasing current density, the spectrum shifts due to added long wavelength content from the LED as well as additional long wavelength components from the red and orange phosphors. The high CCT end also shows a slight upward curve that is caused by saturation of the long wavelength phosphors and more LED light passing through. Shift in the CIE coordinates for the standalone pump source is shown on the bottom left corner of Figure 19. The fact that the direction of shift for the final device and standalone pump differs illustrates that the phosphor emission significantly contributes to the final SPD.

Dual LEDs

First Generation Two Terminal LED Structures

A bright quantum well emission dominated the PL of all samples. Temperature dependent PL data for a blue emitter is shown in Figure 20. Inset shows peak position and intensity as a function of the temperature facilitating the determination of activation energies of 4 meV and 44 meV.

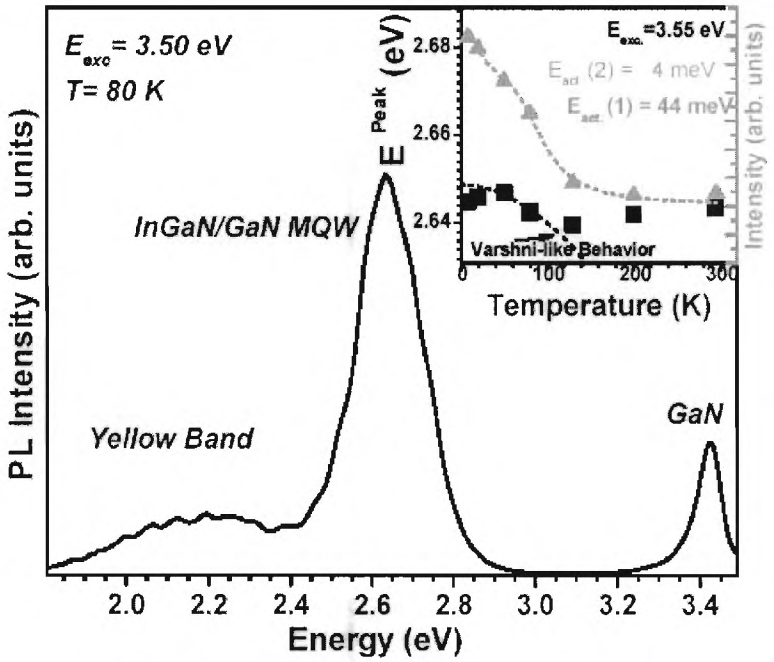

Figure 20. Temperature Dependent PL for blue emitter

Similar results were obtained for the UV emitter (not shown here). A significant S-shape behavior of peak energy, which indicates the presence of QD-like potential fluctuations, is revealed by temperature dependent PL measurements for low excitation energies (Figure 20). Evaluation of MQW emission determines the activation energies to be $E_{act}(1)$ = 4 meV and $E_{act}(2)$ = 44 meV following the approach suggested by Adelmann et al.[12], Equation 3.

$$I = C\left[1 + Ae^{\frac{-E_1}{kT}} + Be^{-E_2 kT}\right] - 1 \qquad (3)$$

where, k is the Boltzmann factor, and A and B are scaling factors. The scaling factor of the latter process is more than 200 times larger than the first. Interface roughness and/or one monolayer fluctuations of the QW thickness typically provide localization centers with localization energies below 5 meV. Therefore, the smaller energy can be attributed to imperfections of the interfaces in the MQW. A more thermally stable localization is indicated by the second E_{act} = 44 meV. It is assigned to the localization of carriers in nanoscale islands caused by fluctuations in the indium concentration. Site selective PL spectroscopy was also performed on the dual MQW device, shown in Figure 21.

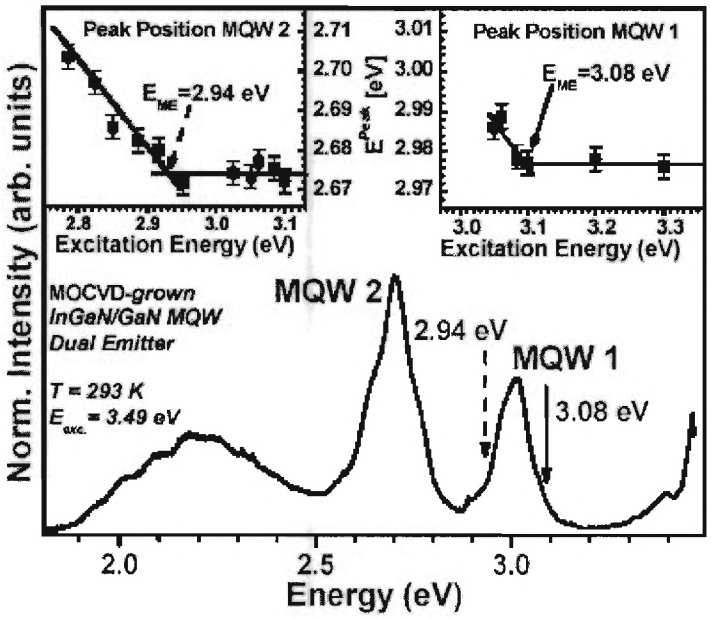

Figure 21. Site Selective PL for MQW device

For each peak a mobility edge can be determined: 2.94 for the blue emission and 3.08 for the UV emission. This indicates the existence of isolated localization sites on the low-energy side of the mobility edges, confirming the radiative recombination in the device is generated in zero dimensional centers. Hence, the dual MQW devices show the same emission mechanism as detected for each single MQW devices.

Bright electroluminescence was also observed from the devices. The EL data for dual MQW region device is shown in Figure 22.

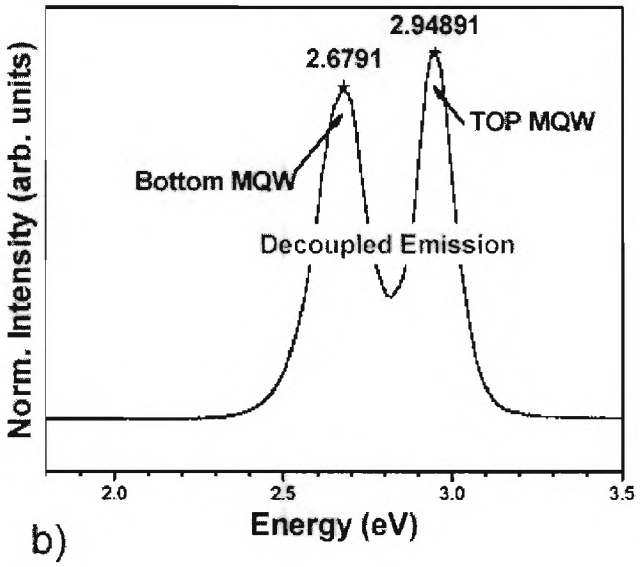

Figure 22. Electroluminescence from a dual LED

Two distinct peaks are observed in the dual MQW region device, showing separate luminescence from each of the MQWs. Similar results are observed for devices with 400 nm and 460 nm peaks.

The enabling light emission mechanism in GaN-based LEDs with a single MQW region, namely carrier localization [13], has been successfully employed in a device with dual MQW regions tailored to emit in the blue and near UV regions of the spectrum. This was important to preserve the same high brightness characteristics from standard GaN LEDs to the new device. Temperature and excitation energy dependent PL measurements confirmed the existence of carrier localization first in the single MQW region devices and then in the dual MQW region devices.

Bright emission derived from the carrier localization is also seen in EL (Figure 22). These devices show that dual wavelength emission is possible from the same device.

Second Generation Two Terminal Dual Wavelength LEDs

First a sample with no doping in any of the barriers was grown, fabricated and tested. The electroluminescent spectra at varied drive current is shown in Figure 23

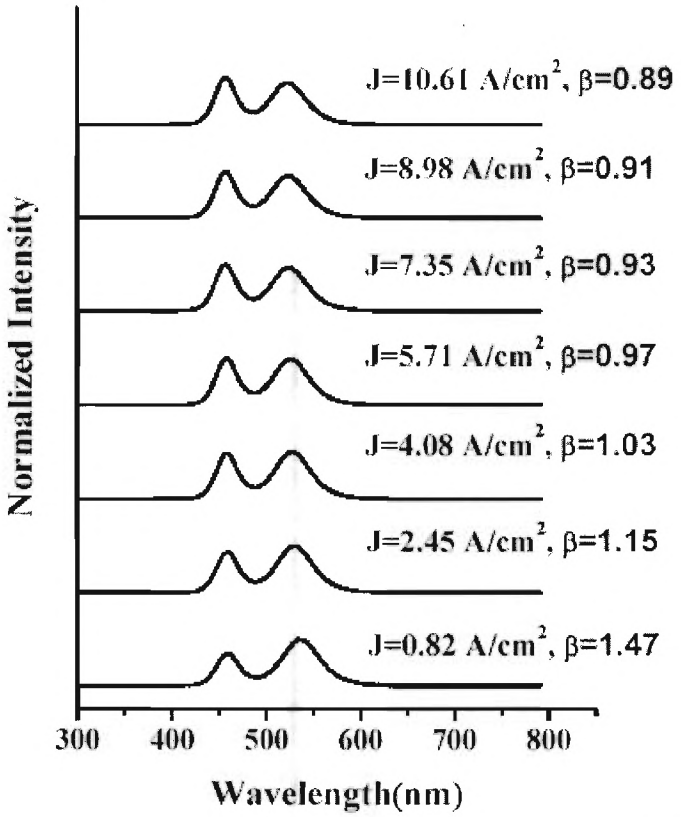

Figure 23. Normalized EL spectra of Dual LED with undoped barriers

Figure 23 shows that at low currents the long wavelength emission is greater than the short wavelength emission. As drive current is increased the relative intensity of the short wavelength emission is increased to a point where the effect saturates. The maximum β for this device is 1.47 and the minimum is 0.89. Next the barrier between QWs 3 and 4 was doped with Si to study the affect it has on the minimum and maximum β. Three samples with different doping levels in the barrier between QWs 3 and 4 were grown, fabricated and tested. The first sample, had a carrier concentration of $6x10^{18}cm^{-3}$ electrons. EL spectra in Figure 24 show that at low currents the short wavelength dominates with a β=0.1.

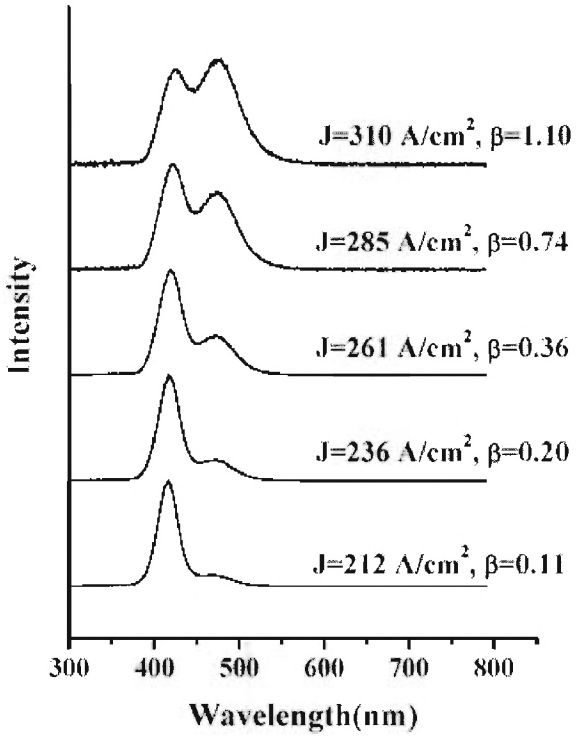

Figure 24. Normalized EL Spectra for $6x10^{18}cm^{-3}$ doped barrier

It is not until very high current densities (220 A/cm^2) that β begins to change. The maximum β reached before the device is destroyed by high current is ~1.1, as shown in Figure 25, where β is plotted against current density.

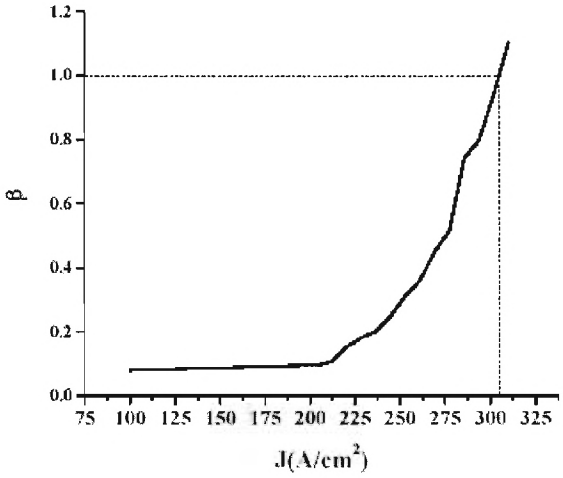

Figure 25. β vs J for $6x10^{18}cm^{-3}$ doped barrier

Another sample was grown with twice the Si doping in the barrier ($1.2x10^{19}cm^{-3}$), however, no change in β was observed for current densities that the device could sustain.

A fourth sample with half the Si doping ($3x10^{18}cm^{-3}$) was also grown. The effect of drive current on β was much greater and started to show at current densities 100 A/cm^2, as seen in Figure 26.

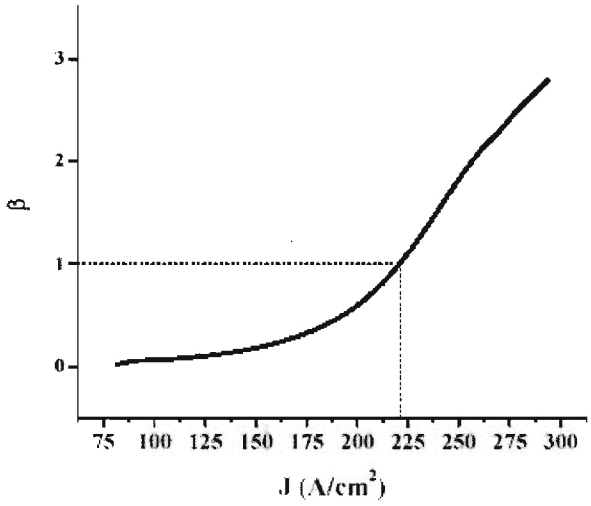

Figure 26. β vs J for $3x10^{18}cm^{-3}$ doped barrier

The maximum β attainable for this device was ~2.5, for which the EL spectrum is shown in Figure 27. The results for these devices are tabulated in Table 5.

Table 5. Summary dual emitter device characteristics

Doping (cm^{-3})	Min β	Max β	β=1
None	0.89	1.47	$4\frac{A}{cm^2}$
3×10^{18}	0.08	2.5	$220\frac{A}{cm^2}$
6×10^{18}	0.08	1.1	$305\frac{A}{cm^2}$
1.2×10^{19}	NA	NA	NA

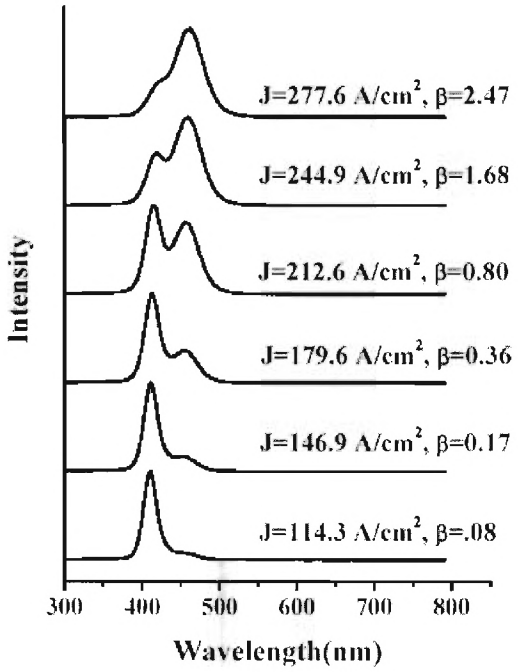

Figure 27. Normalized EL Spectra for $3x10^{18}cm^{-3}$ doped barrier

Discussion of Dual LED

Doping of the barrier between QWs 3 and 4 with Si achieves significant control over the β by varying drive current. A model to explain this behavior considers two barriers to current injection in the different QW regions. A band diagram for the QW region of a device with doping in the barrier between QWs 3 and 4 is shown in Figure 28.

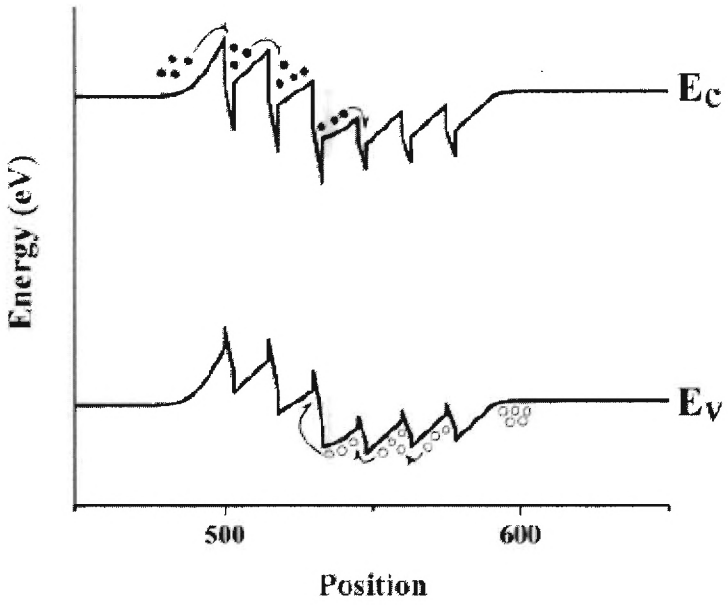

Figure 28. Band Diagram of QW region for a Dual LED with a doped barrier

In Figure 28 the n-type region lies to the left of the QWs and the p-type region is to the right. The relatively high In concentration in the Qws 1-3 leads to electron trapping and blocking, making it more difficult for electrons to travel to QWs 4-6. This effect is best observed in a dual LED with no doping where the QWs 4-6 are preferentially excited at low currents. In the case of no doping holes are more free to move to QWs 1-3 than electrons are to move to QWs 4-6 at low currents. As current is increased the electrons fill higher energy states and are able to travel to QWs 4-6. At this point the mobility of the carrier influences β. QWs 4-6 are more preferentially pumped because holes have lower mobilities and do not travel as far as the electrons, thus recombination is more likely in QWs 4-6. On the other hand, the doping of the barrier between QWs 3 and 4 creates a barrier to hole transport to the QWs 1-3. In the case of the doped barrier the hole blocking washes out the effect of electron blocking at low currents. The holes are trapped in QWs 4-6 until current is high enough to promote some holes over the doped barrier and into QWs 1-3. At this point the electron trapping effect influences β recombination occurs in QWs 1-3.

Conclusion

Several methods for forming a III-nitride tunnel junction were explored, however, a suitable device for a buried current spreading layer was not achieved. Hybrid doping showed the best results as a tunnel junction however the voltage need to achieve reverse currents suitable for LED operation were too high. SPS doping showed strong potential for obtaining high concentrations of holes in p-type material, however, structures incorporating these layers did not create suitable tunnel junctions. Lastly, Mn doping of an intrinsic region in the junction to create defect assisted tunneling also proved to be not suitable for creating a tunnel junction.

The results shown here describe successful use of phosphor combinations with a dual LED to create a dynamic spectrum light source. The first generation phosphor test bed was pumped with a source in which β ranged from 0 to ∞. However, the second generation phosphor test bed had a constraint that it must work with a β range of 0.08 to 2.5. A suitable set of phosphors was used to create a source of which the CCT can be varied from 3228 K to 5339 K by increasing the drive current used in the LED.

A spectrally dynamic broadband source was developed with ability to tune CCT from 3200K to 5300K. The novel use of multiple phosphors which can be selectively excited by two wavelengths of light enabled this development. A two terminal dual LED has been created with the ability to control the relative intensities of the two emission peaks by varying drive current. The development of a three terminal dual LED as a pump source was prohibited by the need for a III-nitride tunnel junction that proved unattainable in the scope of this work. Doping profiles have been used to extend the dynamic range of the two terminal dual LED over other reported devices. Operation of the two terminal dual LEDs is explained as a function of drive current. Combinations of phosphors that have varied excitation spectra provide the ability to selectively excite different phosphors with the different LED emission peaks. First and second generations of the two terminal dual LED and the phosphor combination are discussed. Such innovations may prove important in the success of solid state lighting as a general illumination solution.

The current injection mechanisms for the two terminal dual wavelength LED are not fundamentally different from those of conventional high brightness LEDs. Thus, it is expected that the efficiency of optimized two terminal dual wavelength LED would be near that of other high brightness LEDs. Common enhancement techniques such as chip shaping and flip-chip bonding can be applied to the dual wavelength device as easily as any conventional high brightness LED. Furthermore, if suitable phosphors and pump wavelengths are selected efficiency can be enhanced by minimizing stokes shift seen other phosphor converted white LEDs.

The broadband spectrally dynamic source can be viewed as an enhancement of more conventional LEDs and should exhibit many of the same properties as other high brightness LEDs. This will in part depend on the optimization of drive current control over SPD. With further investigation it is believed that this could be achieved.

References

[1] Lin, Y.-J., "Activation mechanism of annealed mg-doped gan in air," Applied Physics Letters, vol. 84, no. 15, pp. 2760–2762, 2004.

[2] Brennan, K. F., The physics of semiconductors : with applications to optoelectronic devices. Cambridge ; New York: Cambridge University Press, 1999.

[3] Jeon, S. R., Song, Y. H., Jang, H. J., Yang, G. M., Hwang, S. W., and Son, S. J., "Lateral current spreading in gan-based light-emitting diodes utilizing tunnel contact junctions," Applied Physics Letters, vol. 78, no. 21, pp. 3265–3267, 2001.

[4] Diagne, M., He, Y., Zhou, H., Makarona, E., Nurmikko, A. V., Han, J., Waldrip, K. E., Figiel, J. J., Takeuchi, T., and Krames, M., "Vertical cavity violet light emitting diode incorporating an aluminum gallium nitride distributed bragg mirror and a tunnel junction," Applied Physics Letters, vol. 79, no. 22, pp. 3720–3722, 2001. 493CL Times Cited:24 Cited References Count:13.

[5] Meyerhofer, D., Brown, G. A., and Sommers, H. S., "Degenerate germanium .1. tunnel, excess, and thermal current in tunnel diodes," Physical Review, vol. 1, no. 4, pp. 1329–&, 1962. 1471C Times Cited:56 Cited References Count:49.

[6] Kane, E. O., "Theory of tunneling," Journal of Applied Physics, vol. 32, no. 1, p. 3, 1961.

[7] Jeon, S.-R., Oh, C. S., Yang, J.-W., Yang, G. M., and Yoo, B.-S., "Gan tunnel junction as a current aperture in a blue surface-emitting light-emitting diode," Applied Physics Letters, vol. 80, no. 11, p. 1933, 2002.

[8] Chichibu, S., Azuhata, T., Sota, T., and Nakamura, S., "Excitonic emissions from hexagonal gan epitaxial layers," Journal of Applied Physics, vol. 79, no. 5, pp. 2784–2786, 1996.

[9] Takeuchi, T., Sota, S., Katsuragawa, M., Komori, M., Takeuchi, H., Amano, H., and Akasaki, I., "Quantum-confined stark e_ect due to piezoelectric fields in gain strained quantum wells," Japanese Journal of Applied Physics Part 2-Letters, vol. 36, no. 4A, pp. L382–L385, 1997.

[10] Sugawara, M., "Model for lasing oscillation due to bi-excitons and localized biexcitons in wide-gap semiconductor quantum wells," Japanese Journal of Applied Physics, Part 1 (Regular Papers & Short Notes), vol. 35, no. 1A, p. 124, 1996.

[11] O'Donnell, K. P., Martin, R. W., and Middleton, P. G., "Origin of luminescence from ingan diodes," Physical Review Letters, vol. 82, no. 1, pp. 237–240, 1999.

[12] Adelmann, C., Simon, J., Feuillet, G., Pelekanos, N. T., Daudin, B., and Fishman, G., "Self-assembled ingan quantum dots grown by molecular-beam epitaxy," Applied Physics Letters, vol. 76, no. 12, p. 1570, 2000.

[13] Nakamura, S., "The roles of structural imperfections in ingan-based blue light emitting diodes and laser diodes," Science, vol. 281, no. 5379, pp. 956–961, 1998.